Tannin-based hard carbons as high-performance anode materials for sodium-ion batteries

Hélène Tonnoir, D. Huo, Rafael Luan Sehn Canevesi, Vanessa Fierro, Alain Celzard, Raphaël Janot

Tannin-Based Hard-Carbons as High-Performance Anode Materials for Sodium-Ion Batteries

Hélène Tonnoir,[a] Da Huo,[a] Rafael L.S. Canevesi,[b] Vanessa Fierro,[b] Alain Celzard[b] and Raphaël Janot*[a]

[a]Laboratoire de Réactivité et Chimie des Solides (LRCS), CNRS UMR7314,
Université de Picardie Jules Verne,
33 Rue Saint Leu,
80039 Amiens cedex, France
E-mail: raphael.janot@u-picardie.fr

[b]Institut Jean Lamour, CNRS UMR7198,
Université de Lorraine,
Ecole Nationale Supérieure des Technologies et Industries du Bois (ENSTIB),
27 Rue Philippe Séguin,
BP 1041, 88051 Epinal cedex 9, France

Abstract

The demand for efficient and cheap electrochemical storage devices is very high today. Na-ion batteries are emerging as a promising alternative to Li-ion batteries for large-scale applications, due to the much larger abundance of sodium. Among the different negative electrode materials allowing Na insertion at low potentials, hard carbons are the materials with the best electrochemical performances reported so far. Here we investigate the synthesis of hard carbons from tannins, an abundant and cheap bio-sourced carbon precursor made of polyphenolic molecules. We show that by a well-controlled synthesis method and high-temperature pyrolysis (1600°C), a hard carbon with developed ultra-microporosity is obtained. This hard carbon delivers a reversible capacity of 306 mAh g^{-1} at C/20 with a first-cycle coulombic efficiency of 87 %. To our knowledge, these electrochemical performances are among the best ever reported in the literature for biomass-derived hard carbons.

Keywords: Bio-based carbon, Na-ion battery, pyrolysis, coulombic efficiency, porosity, plateau capacity

1. Introduction

In the context of the energy transition, the massive development of renewable energies appears as an efficient way to provide affordable, accessible and sustainable energy sources while acting on climate change [1]. Nevertheless, being intermittent, their production requires finding efficient ways to store energy, both for mobile and stationary applications [2]. Electrochemical energy storage using secondary batteries appears as a good solution. Lithium-ion batteries, in particular, are considered one of the most efficient battery technologies, but

they require quite expensive materials [3]. With similar properties to lithium, sodium is more abundant, evenly distributed on Earth and less expensive [2–5]. Therefore, sodium-ion batteries (SIBs) are a promising alternative to Li-ion batteries for low-cost and stationary applications [2–4,6,7]. Unfortunately, graphite, the common anode material for lithium-ion batteries (with a capacity of 372 mAh g^{-1}), cannot be used in SIBs as sodium shows very poor intercalation into graphite (i.e., formation of a stage 8 compound, NaC_{64}, leading to an electrochemical capacity of only 35 mAh g^{-1}) [8–10]. Several materials, such as tin- or antimony-based alloys [11–13], metal oxides [14–19], organic compounds [20–24], or carbonaceous materials [4,5,8,25–32], have been studied as negative electrode for SIBs. Among them, hard carbons (HC) turn out to be very promising candidates [33,34].

Hard carbons are non-graphitizable carbons composed of randomly oriented turbostratic nano-sized domains, disorganized from one another, giving the material a high ultra-microporosity (i.e., pores size below 1 nm in diameter) [4,5,35]. Such materials are able to store sodium ions with a high reversible capacity (between 250 and 300 mAh g^{-1}), low working potential (vs. Na^+/Na) and good cycling stability [36,37]. Moreover, they are inexpensive and easy to synthesize from many carbonaceous precursors, mainly oxygen-rich molecules and polymers [36] such as, for example, sucrose [5,38,39], glucose [8,26,40], cellulose [6,33,41,42], lignin [2,43], phenolic resins [44–48] or pre-oxidized pitch [34,45,49]. Among all the precursors of hard carbons, those derived from biomass are of great interest lately, such as lignocellulosic biomass and fruit wastes [36,50–57]. About 10 to 15 billion tons of biomass waste are formed worldwide each year. Most of it is not successfully recycled and is generally burnt, which contributes to increased environmental pollution. Transforming biomass, which is a very rich carbon source, into high-value carbonaceous materials for energy storage, is a sustainable way to enhance their recycling [58]. Several bottlenecks still hinder the development of biomass-derived hard carbons for SIBs, namely the variation in chemical composition and seasonal fluctuation of the biomass source, the low carbon yield, and for the obtained hard carbons, the heterogeneous structure, multimodal porosity, too large surface area, and low coulombic efficiency at the first electrochemical cycle [46,59].

Depending on its origin, biomass can have different compositions [60]. In 2017, Dou et al. [53] studied the impact of the composition of three types of biomass: pectin-based with apple waste as a precursor, hemicellulose-based with corncob, and lignin-based using peanut shells. The carbon yields obtained after carbonization were 24.7 %, 33.2 % and 38.2 %, respectively. The fact that the precursor composition has a huge impact on the hard carbon structure and electrochemical performances was emphasized. The HC obtained from peanut shells showed the best performance (reversible capacity of 298 mAh g^{-1} at 20 mA g^{-1} with a coulombic efficiency at first cycle of 68 %). It was concluded that lignocellulose-based biomass showed the most promising performance. In 2020, Saavedra et al. [50] compared the structure and electrochemical performance of hard carbons from three different sources of lignocellulosic biomass: woody biomass (pine as coniferous and beechwood as deciduous), herbaceous

biomass (miscanthus) and agricultural waste (wheat straw). Their study showed that the performance and structure of the resulting hard carbons are more affected by the composition of the initial biomass precursor than by the pyrolysis temperature (1000 to 1400 °C). Indeed, HCs from woody biomass showed lower impurity contents, lower specific surface areas, more turbostratic domains and better performances for all tested temperatures (between 290 and 315 mAh g^{-1} at C/10 (37.2 mA g^{-1}) for pine-derived HC, and between 282 and 309 mAh g^{-1} for beechwood-derived HC). The woody biomass-based HCs also showed coulombic efficiencies above 80 %, while herbaceous and agricultural waste biomass-based HCs showed coulombic efficiencies of only 74 % and 60 %, respectively.

Condensed tannins are polyphenolic biomolecules that are very abundant in nature and, in addition to their low extraction cost, exhibit quite similar reactivity to phenolic molecules of petrochemical origin such as resorcinol [61]. They are also excellent precursors for multiple carbonaceous materials [62] such as cellular [63], mesostructured [64], mesoporous or microporous [65] carbons. Because of their crosslinked and highly aromatic nature, tannin-derived resins maintain their original structure and morphology when submitted to pyrolysis and present an excellent carbon yield (about 47 ± 3%), leading to non-graphitizable glassy carbons [66], currently referred to as "hard carbons" in the context of sodium batteries, but also referred to as vitreous carbons in other contexts. Here, we used condensed tannins from the bark of the Mimosa tree (*Acacia mearnsii*). The carbonization of these precursors and the properties of the corresponding glassy carbons were summarized in [62] and refs. therein, and the details of their rearrangement during pyrolysis were theorized in [67]. In this latter article, we had shown that, after pyrolysis at 900°C, the resulting carbon exhibits a broad distribution of C-C bond lengths centered at 1.42 Å, and that this material can be modelled by a defective structure of bilayer graphene, distorted by defects (residual hetero-elements and non-hexagonal aromatic rings, among others). It was therefore logical to test them for the first time as an electrode for SIBs.

In this work, a series of hard carbons derived from tannins were prepared by a well-controlled synthesis process of polycondensation and pyrolysis. The impact of pyrolysis temperature on the chemical composition, physical properties and electrochemical performance of the HCs was systematically investigated. Compared to other reported biomass-derived HCs, tannin-based HCs exhibit significant improvements in carbon yield, low-voltage plateau capacity, and initial coulombic efficiency. This study shows for the first time the very promising use of tannin-based hard carbons as an anode material for SIBs. The possible origin of its better performance is further discussed in order to help the rational design of other high-performance anode carbon materials.

2. Material and methods

2.1. Hard Carbon Synthesis

A commercial mimosa tannin extract, kindly provided by the company SilvaChimica (St Michele Mondovi, Italy) and available on the market as Fintan OP, was used as a carbon precursor. Cellular vitreous carbon foams were produced from such mimosa extract, co-reacted with furfuryl alcohol and formaldehyde, according to the very general route already detailed elsewhere [68]. Herein, we used to the "standard" formulation when prepared with the specific methodology described elsewhere [69].

Carbonizations were then performed under argon flow (100 mL min^{-1}), placing foam samples in a ceramic boat introduced into an alumina tube (inner diameter 7.5 cm), itself placed in a tubular furnace. The furnace was heated up to the final temperature (900, 1000, 1200, 1400 or 1600 °C) at a rate of 1 °C min^{-1}. The final temperature was held for 1 h, and then the samples were cooled down under argon at a rate of 3 °C min^{-1}.

2.2. Structural and Textural Characterizations

X-Ray Diffraction (XRD) measurements were performed in Bragg-Brentano ϑ-ϑ configuration with a Bruker AXS D8 Advance diffractometer using a copper X-Ray source ($\lambda_{K\alpha}$ = 0.15418 nm) for 2ϑ diffraction angles between 10° and 80°. The XRD patterns were analyzed using the model developed by Mallet-Ladeira [70]. The distance between two graphene layers $d_{(002)}$ was calculated with Bragg's law while Scherrer's formula was used to determine the average lateral size L_a of the graphene domains and the average thickness L_c of the graphene layers stacking.

Raman spectra were recorded with a ThermoScientific microscope DXR Raman spectrometer using an excitation laser of 532 nm wavelength. The power of the laser was set to 1 mW to avoid local heating of the sample. Ten measurements were collected for each sample. For each measurement, the sample was exposed to the laser twice for 30 seconds. The Raman spectra were analyzed using the model developed by Mallet-Ladeira [70], with which the average lateral size L_a of the graphene domains was determined [71]. The quantification of defects in the structure was calculated using the ratio of the integrated area A_D/A_G of the bands D and G.

The textural properties were evaluated by means of nitrogen and hydrogen adsorption isotherms at -196 °C. The physisorption isotherms were performed in a fully automatic 3FLEX (Micromeritics, USA) adsorption device. Outgassing was performed before sample weighing under secondary vacuum at 200 °C, for at least 48 h, in a Micromeritics sample preparation device (Smart VacPrep, Micromeritics). Additionally, the samples were outgassed prior to the adsorption measurements in the 3FLEX unit under secondary vacuum, at 200 °C for at least 12 h. The specific surface area was determined by applying two different methodologies: first the A_{BET} [m^2 g^{-1}] was obtained by applying the BET equation to the nitrogen adsorption data; and the S_{NLDFT} [m^2 g^{-1}] was calculated from both N_2 and H_2 isotherms using the 2D-NLDFT heterogeneous surface model (2D-NLDFT-HS) available on the Saieus® software supplied by Micromeritics. The 2D-NLDFT-HS model was also used to determine the pore size distribution

(PSD) [72] and, by integration of the PSD in the adequate range of pore diameters, the following pore volumes were obtained: ultramicropores (< 0.7 nm), $V_{u\mu}$ [$cm^3\ g^{-1}$]; supermicropores (0.7-2 nm), $V_{s\mu}$ [$cm^3\ g^{-1}$]; micropores (< 2 nm), V_{μ} [$cm^3\ g^{-1}$]; mesopores (2-50 nm), V_{meso} [$cm^3\ g^{-1}$]; and total volume of pores, V_{tot}, [$cm^3\ g^{-1}$]. The surface area provided by micropores and mesopores, S_{μ} [$m^2\ g^{-1}$] and S_{meso} [$m^2\ g^{-1}$], were determined following the PSD integration methodology mentioned previously. The micropore volume and total pore volume, V_{DR} [$cm^3\ g^{-1}$] and $V_{0.97}$ [$cm^3\ g^{-1}$], respectively, were also obtained using the Dubinin-Radushkevich (DR) equation applied to the nitrogen isotherm and the amount of N_2 adsorbed at p/p_0 = 0.97, respectively. The skeletal density of the carbon materials was determined by helium pycnometry using an AccuPyc II 1340 automatic device (Micromeritics, USA) [73].

The elemental content of carbon, hydrogen, nitrogen and sulfur was determined using a Vario EL Cube elemental analyzer (Elementar, Switzerland). The analysis was performed by burning the samples in a stream of pure O_2. The oxygen content was quantified using the same equipment in a second step. More details are given elsewhere [74].

Thermogravimetric Analysis (TGA) was performed using an alumina crucible with a Netzsch STA449C Jupiter machine under air, from 25 °C to 1500 °C with a heating rate of 5 °C min^{-1}.

Scanning Electron Microscopy (SEM) and Energy Dispersion X-ray spectroscopy (EDX) were performed using an FEI Quanta FEG 200 environmental microscope coupled with an Oxford Instrument EDX X-max detector.

2.3. Electrochemistry

2.3.1. Electrode Formulation

The hard carbons were first ground with an agate mortar and then sieved to 20 µm. To prepare the electrode slurry, carboxymethylcellulose (Na-CMC, Acros Organics, average molar mass 700 000 g mol^{-1}), carbon black C45 (Imerys) and Triton X-100 (Tx100, Sigma Aldrich) were used as polymer binder, conductive additive and surfactant, respectively. The slurry was prepared in aqueous formulation (92 wt. % HC / 2.6 wt. % CMC / 2.9 wt. % C45 / 2.5 wt. % Tx100) and was stirred with a magnetic stirrer for 5 h. Then, the slurry was applied to an aluminum foil (20 µm thick) using a doctor blade (300 µm gap). After coating, the film was dried at 100 °C for 1 h. The electrodes of 15 mm diameter were dried at 110 °C overnight under vacuum in a Büchi glass oven. The loading of active material was around 3 mg cm^{-2}.

2.3.2. Half-Cell Galvanostatic Cycling

Electrochemical studies were carried out in two-electrode coin cells (CR2032) using HC as working electrode, sodium metal (Sigma Aldrich) as counter and reference electrode, a solution of sodium hexafluorophosphate ($NaPF_6$, Stella Chemicals, 1 mol L^{-1}) in a mix of ethylene carbonate and dimethyl carbonate (EC/DMC, DodoChem, 50:50 by mass) as electrolyte, and glass fiber separator (Whatman). The coin cells were cycled between 0 and

2.5 V (vs Na^+/Na) at C/20 (18.6 mA g_{carbon}^{-1}) for 10 cycles and C/10 for 100 cycles. A C-rate of C/n corresponds to the intercalation of one Na^+ ion into the carbon in n hours. The C-rates are calculated considering the hypothetical formation of a NaC_6 phase during sodiation with a theoretical specific capacity of 372 mAh g^{-1}.

2.3.3. Full-Cell Galvanostatic Cycling

The HC was then tested in a full cell configuration versus $Na_3V_2(PO_4)_3$ (NVP) in order to perform rate capability test and long cycling. The cathode was formulated using polyvinylidene difluoride (PVdF, Solvay) as polymer binder and carbon black C45 (Imerys) as conductive additive. The slurry was prepared in organic formulation (92 wt. % NVP / 4 wt. % PVdF / 4 wt. % C45, in N-Methyl-2-pyrrolidone (NMP, BASF)). The cathode was deposited on Al foil (20 µm thick) and calendered to decrease the electrode porosity to about 40 %. Coin cells were assembled using HC as anode and NVP as cathode. The capacity ratio of the negative electrode to the positive electrode was 1.3/1. The C-rate and associated currents were calculated for NVP with a theoretical specific capacity of 118 mAh g^{-1}. The coin cells were cycled between 2.0 and 3.8 V for 5 cycles at each of the following rates: C/5 (23.5 mA g_{NVP}^{-1}), C/2, C, 2C, 3C and, finally, at C/5 for the subsequent cycles. For long cycling, the coin cells were cycled between 2.0 and 3.8 V for 5 cycles at C/5 and then for 1000 cycles at C/2.

3. Results and discussion

3.1. Impact of the Pyrolysis Temperature on Structure, Texture and Composition

The hard carbons were synthesized by pyrolysis of tannin-based carbon foams at five different temperatures: 900 °C, 1000 °C, 1200 °C, 1400 °C and 1600 °C. The obtained hard carbons were denoted by *HCX* (*X* being the pyrolysis temperature). In order to study the impact of pyrolysis temperature on the structure of the hard carbons, X-Ray Diffraction (XRD) and Raman spectroscopy analysis were carried out for the five samples.

For all pyrolysis temperatures, the shapes of the XRD patterns are very similar and typical of hard carbons (Fig. 1.a). A first broad peak (002) located around 2ϑ = 23° is related to the spacing between graphene layers in the turbostratic domains and a second broad peak (10*l*) located around 2ϑ = 44° is associated with the contributions of the (100), (101) and (004) reflections [3]. As the temperature of pyrolysis increases, a slight decrease in the interlayer spacing from 0.39 nm to 0.37 nm is noticed. Few differences were observed for the lateral size of the graphene domains, L_a, and the thickness of the graphene layers stacking, L_c, with the increase in pyrolysis temperature (Table S1). The XRD patterns show impurities at $2\vartheta \approx 31°$, especially for *HC1600*. Those impurities were identified by Scanning Electron Microscopy (SEM) and Energy Dispersive X-ray spectroscopy (EDX) as mainly composed of potassium and sulfur (Fig. S1). The former is a common impurity in tannins [61], which, as we recall, are tree bark extracts, and the latter comes from the catalyst used to crosslink the tannin-based resin, i.e., paratoluene sulfonic acid. However, these two elements are in low amount in the hard

carbon material: 2.1 wt. %, as shown by the residual mass observed by thermogravimetric analysis up to 1500 °C under air flow (Fig. S2).

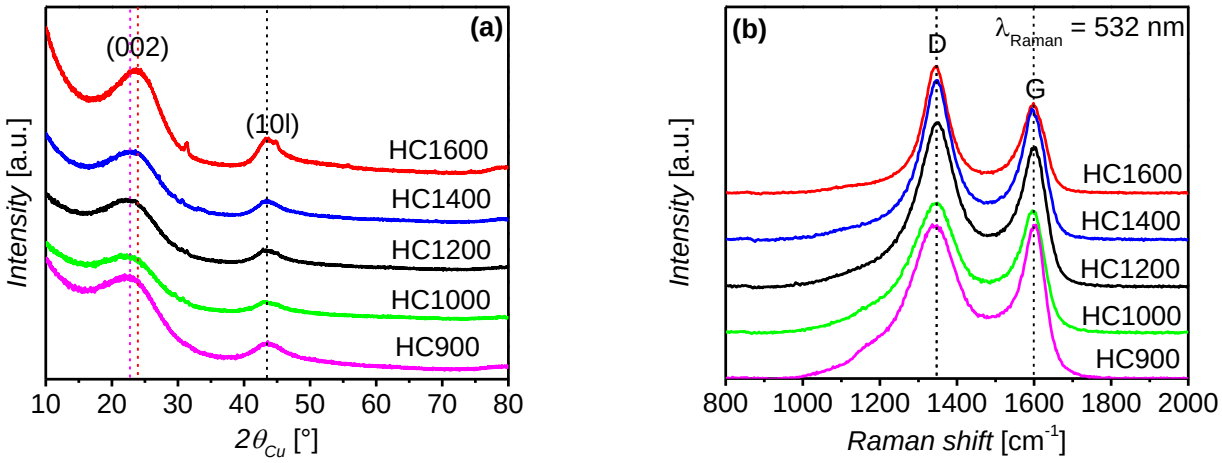

Fig. 1 (a) XRD patterns and (b) Raman spectra of tannin-derived HCs pyrolyzed at different temperatures.

The Raman spectra obtained for the five samples are presented in Fig. 1.b. All first-order Raman spectra show two bands: the D-band, around 1350 cm^{-1}, associated with structural defects in the material, and the G-band, around 1600 cm^{-1}, associated with turbostratic domains [3]. For all pyrolysis temperatures, the shapes of the spectra are very similar. The Raman shifts remain the same as the temperature of pyrolysis increases but the bands become sharper. As the temperature of pyrolysis increases, the lateral size of the graphene domains L_a increases from 5.5 to 6.7 nm and the ratio of integrated areas of D and G bands A_D/A_G related to the quantity of defects in the material decreases from 2.36 to 1.55 (Table S1). This shows that the crystallinity of the material increases with the pyrolysis temperature, although the hard carbon remains non-graphitizable.

Further characterizations were performed to probe the texture and porosity of the materials. Nitrogen adsorption/desorption was used to determine the Brunauer-Emmett-Teller (BET) specific area, and helium pycnometry was used to determine the skeletal density of the material. The results are presented in Fig. 2.a.

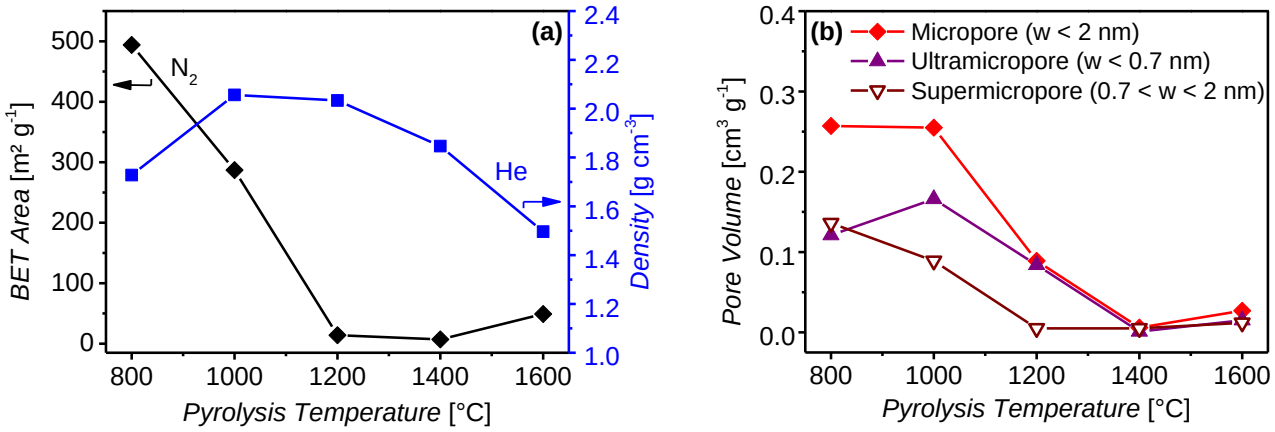

Fig. 2 (a) Evolution of BET area (from N_2 adsorption at -196 °C) and materials' skeletal density (from helium pycnometry), and (b) Evolution of pore volumes as a function of pyrolysis temperature (from N_2 and H_2 adsorption at -196 °C).

The BET area, A_{BET}, decreases strongly with the increase of the pyrolysis temperature (from 287 $m^2\ g^{-1}$ for *HC1000* to 7 $m^2\ g^{-1}$ for *HC1400*), becoming very low at temperatures above 1200 °C (Table S2). This is related to the removal of structural defects and the closure of the porosity accessible to N_2 molecules. At the same time, the carbon skeletal density, measured by He pycnometry, first increases up to 2.05 g cm^{-3} at 1000 °C, then decreases to 1.48 g cm^{-3} at 1600 °C. This two-step evolution can be explained, in a first step, by an organization of the polyaromatic units and a decrease of the interlayer spacing and, in a second step, by the decrease of the pore size and the formation of ultra-micropores, which are inaccessible to He, and which, consequently, decrease the skeletal density. These observations, derived from adsorption and pycnometry measurements, are consistent and can be related to the decrease in pore size, as micropores become inaccessible to N_2 and He with increasing pyrolysis temperature.

In order to gain further insight into the microporosity of the carbon materials, hydrogen adsorption/desorption was performed at -196 °C. Hydrogen is supercritical at this temperature and has a molecular diameter of 0.296 nm, whereas that of nitrogen is 0.358 nm. Hydrogen therefore diffuses faster than nitrogen and can penetrate smaller pores. In addition, the hydrogen molecule has a small quadrupole moment, which makes it less sensitive than nitrogen to the surface chemistry of carbon materials. Thus, when hydrogen and nitrogen adsorption data are used in combination, they can provide meaningful pore size distribution (PSD) results over a wide range of pore sizes [72]. Therefore, V_{tot} and V_{μ}, calculated using both isotherms are higher than $V_{0.97}$ and V_{DR}, respectively, determined from the nitrogen isotherm alone. Table S3 shows that the carbon textures are mainly microporous (i.e., pore size less than 2 nm) and that as the pyrolysis temperature increases, the total pore volume in the structure decreases from 0.255 $cm^3\ g^{-1}$ for *HC1000* to 0.008 $cm^3\ g^{-1}$ for *HC1400* and then slightly increases to 0.038 $cm^3\ g^{-1}$ for *HC1600* (Table S3). Moreover, Fig. 2.b shows that the amount of ultra-micropores (with size less than 0.7 nm) increases while the amount of super-

micropores (size between 0.7 nm and 2 nm) decreases when the pyrolysis temperature increases.

Fig. 3.a shows that the porosity of *HC1000* is bimodal and becomes unimodal at higher temperature. Fig. 3.a and b show that the amount of small micropores in the material decreases as the temperature of pyrolysis increases from 1000 °C to 1400 °C. Thus, the average pore and micropore diameters (w_0 and w_μ respectively) increase (Table S3). *HC1000* and *HC1200* are exclusively microporous with an average pore diameter of 0.63 and 0.60 nm, respectively (Table S3). For *HC1400*, w_0 increases to 1.32 nm and w_μ increases to 0.94 nm. For *HC1600*, some micropores and mesopores develop in the structure, leading to a decrease in w_0 and w_μ to 1.31 nm and 0.84 nm, respectively (Table S3).

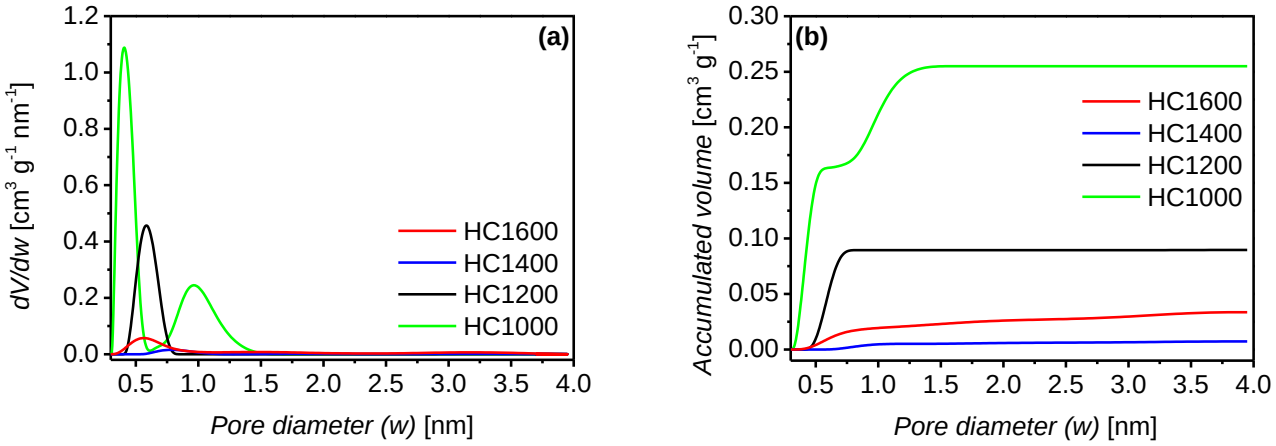

Fig. 3 (a) Pore size distributions in volume (derived from N_2 and H_2 adsorption at -196 °C), and (b) Cumulated pore volumes as a function of pore diameter (derived from N_2 and H_2 adsorption at -196 °C).

Elemental analysis was also performed to follow the evolution of the material composition with the increase of the temperature of pyrolysis (Table S4). This characterization showed a strong decrease in the amounts of heteroatoms (H, O, N, S) as the pyrolysis temperature increased (from ~ 7 wt. % for *HC900* to ~ 1 wt. % for *HC1600*). Especially, the oxygen content dropped from 4.5 wt. % for *HC900* to 0.6 wt. % for *HC1600*, showing that O atoms were eliminated at high temperatures. The hydrogen content is mainly correlated with the C-H bonds at the edges of the graphene layers. As the pyrolysis temperature increased, the hydrogen content decreased from 0.64 wt. % (7.36 at. %) for *HC900* to 0.09 wt. % (1.12 at. %) for *HC1600,* showing a strong decrease in the number of graphene edges. This is correlated with the decrease in the number of structural defects and the increase in the size of the turbostratic domains (L_a and L_c), as previously observed by X-ray diffraction and Raman spectroscopy. Interestingly, the decrease in H content could also be related to the removal of surface groups (-OH, -COOH). The latter is particularly important for the subsequent decrease

in Solid Electrolyte Interphase (SEI) formation and the reduction of the irreversible capacity during the first electrochemical cycle.

3.2. Impact of the Pyrolysis Temperature on the Electrochemical Performance

The electrochemical performance of the HCs electrodes was characterized in half-cells with metallic sodium as counter and reference electrode. Fig. 4 shows the evolution of the galvanostatic profiles with the pyrolysis temperature in a voltage range of 0 to 2.5 V (vs. Na^+/Na) at a current rate of C/20. The electrochemical profiles can be divided in two regions: the sloping region between 2.5 V and 0.1 V (vs Na^+/Na), and the plateau region below 0.1 V (vs Na^+/Na). These profiles are correlated with the storage mechanism of sodium ions in hard carbons. Two mechanisms are mainly considered in the literature. The first one was proposed in 2000 by Stevens and Dahn by comparison with lithium storage in hard carbons [26]. They associated the sloping region of the galvanostatic profile with the intercalation of sodium between the graphene layers in the turbostratic domains, and the plateau region with the filling of micropores by sodium [8,26,75]. The second one, proposed in 2015 by Bommier et al. and others, associates the sloping region with the adsorption of sodium ions on structural defects, and the plateau region with the intercalation of sodium in turbostratic domains and micropore filling [5]. Numerous studies were then conducted to confirm/refute and/or complement the two proposed mechanisms [2]. In view of the many contradictory observations made, the mechanism has not yet been clearly resolved, but three phenomena are involved: sodium ion adsorption on structural defects and heteroatoms, sodium ion intercalation between graphene layers, and micropore filling [3].

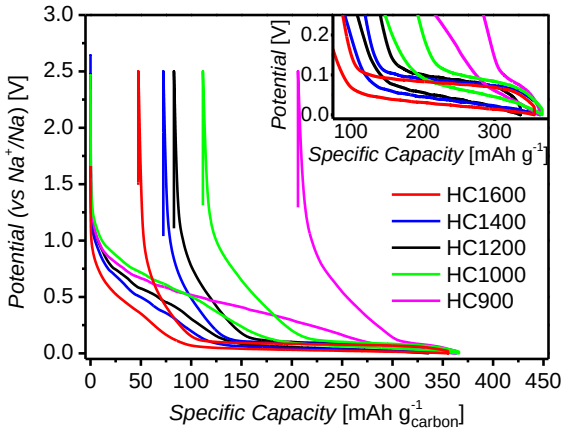

Fig. 4. Evolution of the galvanostatic profiles with the increase of the pyrolysis temperature at C/20 (18.6 mA g_{carbon}^{-1}). In insert, zoom on the low voltage region (0.0-0.25 V vs. Na^+/Na) to better visualize the plateau region and the polarization between charge and discharge.

The insert in Fig. 4 shows that as the pyrolysis temperature increases, the polarization remains similar (~ 45 mV) but the low-voltage plateau capacity increases a lot. Fig. 5 shows the evolution of the reversible capacity, sloping region and plateau region capacities, and coulombic efficiency at the first cycle with pyrolysis temperature.

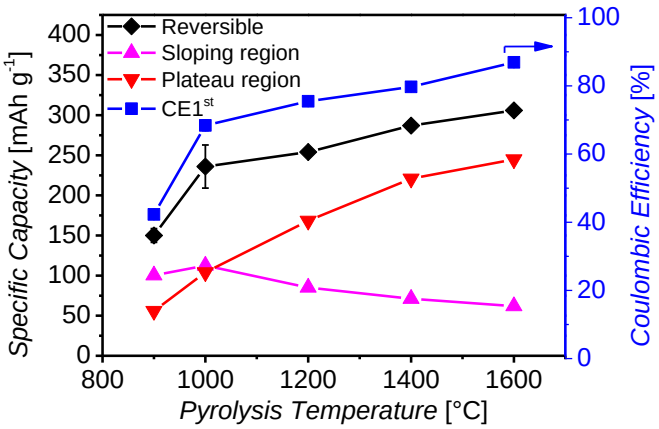

Fig. 5. Evolution of the electrochemical performances as a function of pyrolysis temperature at C/20.

Fig. 5 shows that the electrochemical performance of the hard carbons increases with the temperature of pyrolysis. Indeed, the reversible capacity and coulombic efficiency increase from 150 mAh g^{-1} with a first-cycle coulombic efficiency of 42 % for the hard carbon pyrolyzed at 900 °C to 306 mAh g^{-1} with a first-cycle coulombic efficiency of 87 % for that pyrolyzed at 1600 °C. The carbon pyrolyzed at 1600 °C shows high electrochemical performance for use in sodium-ion batteries, among the best ever reported in the literature for a bio-based hard carbon (Table S5). It is worth noting that *HC1600* exhibits an ultra-high low-voltage plateau capacity of 245 mAh g^{-1}, which represents 80 % of the total reversible capacity.

As the pyrolysis temperature increases, the plateau region capacity increases from 56 mAh g^{-1} to 245 mAh g^{-1} while the sloping region capacity decreases from 100 mAh g^{-1} to 62 mAh g^{-1} for *HC900* and *HC1600*, respectively. This can be related to the structural observations discussed in the first part of the paper. In general, to minimize the irreversible capacity, the BET area must be very low (typically less than 10 m^2 g^{-1}), but *HC1600* shows an A_{BET} of 49 m^2 g^{-1} (Table S2). Thus, the decrease in irreversibility at high temperature seems to be rather related to the decreases in both the heteroatom content, as determined by elemental analysis (Table S4), and the number of structural defects, as observed by XRD and Raman spectroscopy (Table S1). At high pyrolysis temperature, the skeletal density measured by He pycnometry decreases as the pore volume decreases (Table S3): for *HC1600*, the porosity is mainly ultra-microporous (71 % of the total pore volume). Thus, the increase in the plateau region capacity could be correlated with the reduction in pore size with the increase in pyrolysis temperature. In view of these observations, the plateau region appears to be correlated with the filling of micropores by sodium.

The use of sodium metal as anode in half-cell configuration using alkyl carbonate electrolytes leads to a rapid decrease in capacity due to the Solid Electrolyte Interphase (SEI) and to the Na counter electrode itself [76]. Thus, it is difficult to predict the electrochemical performance of the HC from half-cell to full-cell in terms of electrode longevity [77,78]. Therefore, power

rate test and long cycling were performed for *HC1600* in a full-cell configuration versus $Na_3V_2(PO_4)_3$ (NVP) as the cathode. As shown in Figure S3, NVP has a very well defined plateau at 3.4 V (vs Na^+/Na). To avoid Na plating, the full-cells were balanced with 30 % excess of negative electrode. Fig. 6 shows the results obtained for the power test in full cell configuration. The first cycles obtained at C/5 (23.5 mA g_{NVP}^{-1}) are shown in Fig. 6.a. The reversible capacity (i.e., initial discharge capacity) of the full cell is 81 mAh g_{NVP}^{-1} with a coulombic efficiency at the first cycle of 67 %. The lower 1st cycle coulombic efficiency observed in full cell could be attributed to the formation of Cathode Electrolyte Interphase (CEI) on the surface of the cathode material. Moreover, the performance obtained in half-cell for NVP with sodium as counter electrode (Fig. S3) is low (about 100 mAh g^{-1} for the reversible capacity and 68 % for the initial coulombic efficiency at C/5 (23.5 mA g_{NVP}^{-1})). Furthermore, the electrolyte formulation was not optimized by using additives or varying its composition in order to stabilize the SEI and achieve better cycling performance [79,80].

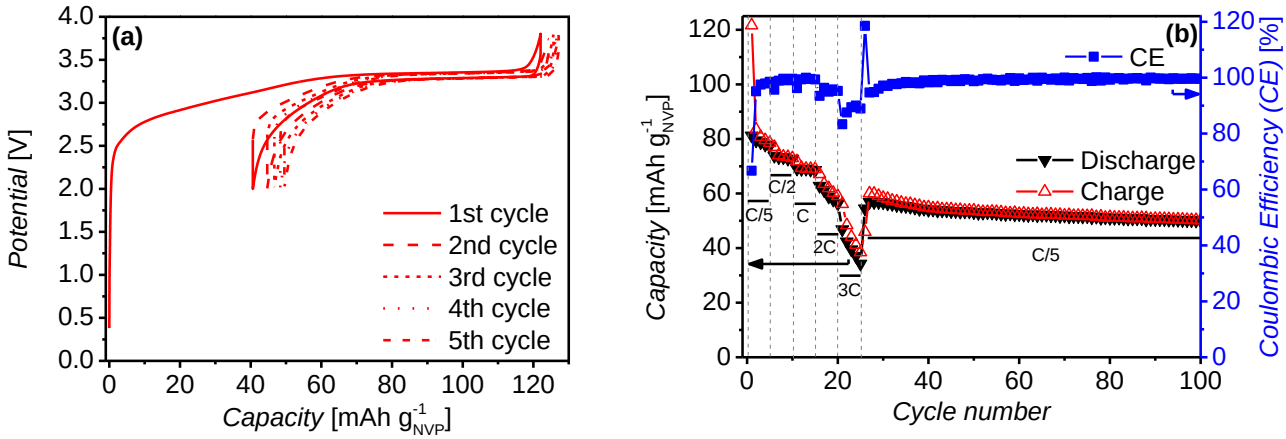

Fig. 6 (a) Galvanostatic profiles of *HC1600* vs NVP at C/5 (23.5 mA g_{NVP}^{-1}): first five cycles. The excess of negative electrode is 30%. (b) Rate capability of *HC1600* vs NVP.

Fig. 6.b shows the rate capability of the material vs NVP. At low rate, the capacity remains quite stable: the discharge capacity retention is around 97 % of the initial capacity at C/5 (around 78 mAh g^{-1}), around 90 % (72 mAh g^{-1}) at C/2 and 85 % (69 mAh g^{-1}) at C. For higher rates (2C and 3C), the discharge capacity retention drops from 77 % (63 mAh g^{-1}, first cycle at C/2) to 42 % (34 mAh g^{-1}, last cycle at 3C). After returning to C/5, the battery recovers about 70 % of its initial capacity (57 mAh g^{-1}) and, after 100 cycles, the discharge capacity retention is around 62 % (50 mAh g^{-1}). In order to study the longevity of *HC1600*, a long cycling test was performed (Fig. 7). The battery was first cycled at C/5 for five cycles to allow for SEI formation and then cycled at C/2 for 50 more cycles. After 50 cycles, the battery shows 82 % capacity retention (90 % capacity retention compared to the first cycle at C/2).

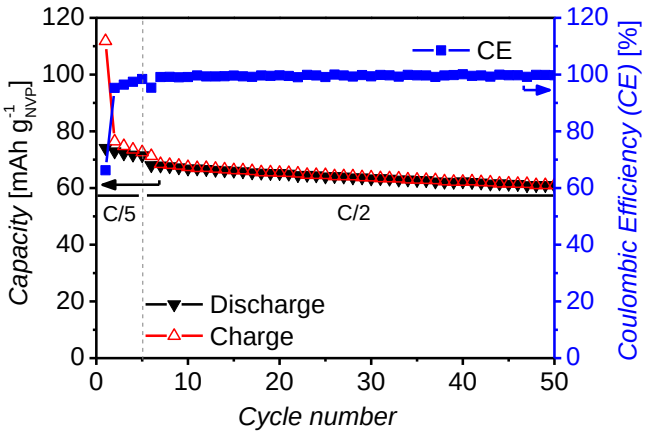

Fig. 7. Long cycling performance of *NVP* / *HC1600* full cell at C/5 for 5 cycles and C/2 for 50 cycles.

4. Conclusions

This study reported on a series of novel bio-based hard carbons using tannin as carbonaceous precursor and investigated for applications as anode for sodium-ion batteries. The impacts of pyrolysis temperature on the structure, texture, composition and electrochemical performance of the carbon materials were studied. With the increase of pyrolysis temperature, the crystallinity of the hard carbons increases, whereas the BET area, skeletal density, heteroatom content and pore size decrease. The electrochemical tests showed a strong increase in the performance of the material, especially an increase in the plateau region capacity with the increase of pyrolysis temperature. Interestingly, the hard carbon obtained at 1600 °C shows a high reversible capacity (306 mAh g^{-1}) at C/20 as well as a high initial coulombic efficiency (87 %). To our knowledge, such electrochemical performances are among the best ever reported in the literature for a hard carbon derived from biomass.

Acknowledgements

This work was supported by the French Ministry of Higher Education, Research and Innovation (Ministère de l'Enseignement Supérieur, de la Recherche et de l'Innovation (MESRI)) and the TALiSMAN project funded by the European Regional Development Funds (ERDF). The authors warmly thank François Rabuel (LRCS) for his help in the formulation and calendering of the cathode, Matthieu Courty (LRCS) for the TGA measurements, and Philippe Gadonneix (IJL) for the foam carbonization.

References

[1] S. Chu, A. Majumdar, Opportunities and challenges for a sustainable energy future, Nature. 488 (2012) 294–303. https://doi.org/10.1038/nature11475.

[2] S. Alvin, D. Yoon, C. Chandra, H.S. Cahyadi, J.H. Park, W. Chang, K.Y. Chung, J. Kim, Revealing sodium ion storage mechanism in hard carbon, Carbon N. Y. 145 (2019) 67–

81. https://doi.org/10.1016/j.carbon.2018.12.112.
[3] X. Dou, I. Hasa, D. Saurel, C. Vaalma, L. Wu, D. Buchholz, D. Bresser, S. Komaba, S. Passerini, Hard carbons for sodium-ion batteries: Structure, analysis, sustainability, and electrochemistry, Mater. Today. 23 (2019) 87–104. https://doi.org/10.1016/j.mattod.2018.12.040.
[4] D. Saurel, B. Orayech, B. Xiao, D. Carriazo, X. Li, From Charge Storage Mechanism to Performance : A Roadmap toward High Specific Energy Sodium-Ion Batteries through Carbon Anode Optimization, Adv. Energy Mater. 1703268 (2018) 1–33. https://doi.org/10.1002/aenm.201703268.
[5] C. Bommier, T.W. Surta, M. Dolgos, X. Ji, New Mechanistic Insights on Na-Ion Storage in Nongraphitizable Carbon, Nano Lett. 15 (2015) 5888–5892. https://doi.org/10.1021/acs.nanolett.5b01969.
[6] C. Matei Ghimbeu, J. Górka, V. Simone, L. Simonin, S. Martinet, C. Vix-Guterl, Insights on the Na+ ion storage mechanism in hard carbon: Discrimination between the porosity, surface functional groups and defects, Nano Energy. 44 (2018) 327–335. https://doi.org/10.1016/j.nanoen.2017.12.013.
[7] J.M. Stratford, P.K. Allan, O. Pecher, A. Chater, C.P. Grey, Mechanistic insights into sodium storage in hard carbon anodes using local structure probes, Chem. Commun. 52 (2016) 12430–12433. https://doi.org/10.1039/C6CC06990H.
[8] D.A. Stevens, J.R. Dahn, The Mechanisms of Lithium and Sodium Insertion in Carbon Materials, J. Electrochem. Soc. 148 (2001) A803. https://doi.org/10.1149/1.1379565.
[9] Y. Liu, B. V. Merinov, W.A. Goddard, Origin of low sodium capacity in graphite and generally weak substrate binding of Na and Mg among alkali and alkaline earth metals, Proc. Natl. Acad. Sci. U. S. A. 113 (2016) 3735–3739. https://doi.org/10.1073/pnas.1602473113.
[10] N. Yabuuchi, K. Kubota, M. Dahbi, S. Komaba, Research development on sodium-ion batteries, Chem. Rev. 114 (2014) 11636–11682. https://doi.org/10.1021/cr500192f.
[11] L. Xiao, Y. Cao, J. Xiao, W. Wang, L. Kovarik, Z. Nie, J. Liu, High capacity, reversible alloying reactions in SnSb/C nanocomposites for Na-ion battery applications, Chem. Commun. 48 (2012) 3321–3323. https://doi.org/10.1039/c2cc17129e.
[12] J. Qian, Y. Chen, L. Wu, Y. Cao, X. Ai, H. Yang, High capacity Na-storage and superior cyclability of nanocomposite Sb/C anode for Na-ion batteries, Chem. Commun. 48 (2012) 7070–7072. https://doi.org/10.1039/c2cc32730a.
[13] Y. Xu, Y. Zhu, Y. Liu, C. Wang, Electrochemical performance of porous carbon/tin composite anodes for sodium-ion and lithium-ion batteries, Adv. Energy Mater. 3 (2013) 128–133. https://doi.org/10.1002/aenm.201200346.
[14] H. Pan, X. Lu, X. Yu, Y.S. Hu, H. Li, X.Q. Yang, L. Chen, Sodium storage and transport properties in layered Na2Ti 3O7 for room-temperature sodium-ion batteries, Adv. Energy Mater. 3 (2013) 1186–1194. https://doi.org/10.1002/aenm.201300139.
[15] Y. Ge, H. Jiang, J. Zhu, Y. Lu, C. Chen, Y. Hu, Y. Qiu, X. Zhang, High cyclability of carbon-coated TiO2 nanoparticles as anode for sodium-ion batteries, Electrochim. Acta. 157 (2015) 142–148. https://doi.org/10.1016/j.electacta.2015.01.086.
[16] S. Hariharan, K. Saravanan, P. Balaya, α-MoO3: A high performance anode material for sodium-ion batteries, Electrochem. Commun. 31 (2013) 5–9. https://doi.org/10.1016/j.elecom.2013.02.020.
[17] D. Su, H.J. Ahn, G. Wang, SnO2@graphene nanocomposites as anode materials for Na-ion batteries with superior electrochemical performance, Chem. Commun. 49 (2013)

3131–3133. https://doi.org/10.1039/c3cc40448j.
[18] Q. Sun, Q.Q. Ren, H. Li, Z.W. Fu, High capacity Sb2O4 thin film electrodes for rechargeable sodium battery, Electrochem. Commun. 13 (2011) 1462–1464. https://doi.org/10.1016/j.elecom.2011.09.020.
[19] P. Senguttuvan, M.R. Palacín, G. Rousse, V. Seznec, J.-M. Tarascon, Na 2 Ti 3 O 7 : Lowest Voltage Ever Reported Oxide Insertion Electrode for Sodium Ion Batteries, Chem. Mater. 23 (2011) 4109. https://doi.org/10.1021/cm202076g
[20] Q. Zhao, Y. Lu, J. Chen, Advanced Organic Electrode Materials for Rechargeable Sodium-Ion Batteries, Adv. Energy Mater. 7 (2017). https://doi.org/10.1002/aenm.201601792.
[21] Y. Park, D.S. Shin, S.H. Woo, N.S. Choi, K.H. Shin, S.M. Oh, K.T. Lee, S.Y. Hong, Sodium terephthalate as an organic anode material for sodium ion batteries, Adv. Mater. 24 (2012) 3562–3567. https://doi.org/10.1002/adma.201201205.
[22] L. Zhao, J. Zhao, Y.S. Hu, H. Li, Z. Zhou, M. Armand, L. Chen, Disodium terephthalate (NA2C8H4O4) as high performance anode material for low-cost room-temperature sodium-ion battery, Adv. Energy Mater. 2 (2012) 962–965. https://doi.org/10.1002/aenm.201200166.
[23] H. Ha, S. Nam, S.H. Jeong, S. Hyun, Development of covalent-bonded organic/carbon anode for sodium-ion battery, J. Mech. Sci. Technol. 33 (2019) 3865–3870. https://doi.org/10.1007/s12206-019-0730-2.
[24] V.A. Oltean, S. Renault, M. Valvo, D. Brandell, Sustainable materials for sustainable energy storage: Organic Na electrodes, Materials (Basel). 9 (2016). https://doi.org/10.3390/ma9030142.
[25] H.S. Moon, J.H. Lee, S. Kwon, I.T. Kim, S.G. Lee, Mechanisms of na adsorption on graphene and graphene oxide: Density functional theory approach, Carbon Lett. 16 (2015) 116–120. https://doi.org/10.5714/CL.2015.16.2.116.
[26] D.A. Stevens, J.R. Dahn, High Capacity Anode Materials for Rechargeable Sodium-Ion Batteries, J. Electrochem. Soc. 147 (2000) 1271. https://doi.org/10.1149/1.1393348.
[27] Y. Cao, L. Xiao, M.L. Sushko, W. Wang, B. Schwenzer, J. Xiao, Z. Nie, L. V. Saraf, Z. Yang, J. Liu, Sodium ion insertion in hollow carbon nanowires for battery applications, Nano Lett. 12 (2012) 3783–3787. https://doi.org/10.1021/nl3016957.
[28] S. Komaba, W. Murata, T. Ishikawa, N. Yabuuchi, T. Ozeki, T. Nakayama, A. Ogata, K. Gotoh, K. Fujiwara, Electrochemical Na insertion and solid electrolyte interphase for hard-carbon electrodes and application to Na-ion batteries, Adv. Funct. Mater. 21 (2011) 3859–3867. https://doi.org/10.1002/adfm.201100854.
[29] Z. Jian, C. Bommier, L. Luo, Z. Li, W. Wang, C. Wang, P.A. Greaney, X. Ji, Insights on the Mechanism of Na-Ion Storage in Soft Carbon Anode, Chem. Mater. 29 (2017) 2314–2320. https://doi.org/10.1021/acs.chemmater.6b05474.
[30] W. Luo, Z. Jian, Z. Xing, W. Wang, C. Bommier, M.M. Lerner, X. Ji, Electrochemically expandable soft carbon as anodes for Na-ion batteries, ACS Cent. Sci. 1 (2015) 516–522. https://doi.org/10.1021/acscentsci.5b00329.
[31] X.F. Luo, C.H. Yang, J.K. Chang, Correlations between electrochemical Na+ storage properties and physiochemical characteristics of holey graphene nanosheets, J. Mater. Chem. A. 3 (2015) 17282–17289. https://doi.org/10.1039/c5ta03687a.
[32] J. Wan, F. Shen, W. Luo, L. Zhou, J. Dai, X. Han, W. Bao, Y. Xu, J. Panagiotopoulos, X. Fan, D. Urban, A. Nie, R. Shahbazian-Yassar, L. Hu, In situ transmission electron microscopy observation of sodiation-desodiation in a long cycle, high-capacity

reduced graphene oxide sodium-ion battery anode, Chem. Mater. 28 (2016) 6528–6535. https://doi.org/10.1021/acs.chemmater.6b01959.
[33] A. Beda, C. Villevieille, P.L. Taberna, P. Simon, C. Matei Ghimbeu, Self-supported binder-free hard carbon electrodes for sodium-ion batteries: Insights into their sodium storage mechanisms, J. Mater. Chem. A. 8 (2020) 5558–5571. https://doi.org/10.1039/c9ta13189b.
[34] N. Daher, D. Huo, C. Davoisne, P. Meunier, R. Janot, Impact of Preoxidation Treatments on Performances of Pitch-Based Hard Carbons for Sodium-Ion Batteries, ACS Appl. Energy Mater. 3 (2020) 6501–6510. https://doi.org/10.1021/acsaem.0c00727.
[35] M.M. Titirici, H. Alptekin, H. Au, A.C.S. Jensen, E. Olsson, M. Goktas, T.F. Headen, P. Adelhelm, Q. Cai, A.J. Drew, Sodium storage mechanism investigations through structural changes in hard carbons, ACS Appl. Energy Mater. 3 (2020) 9918–9927. https://doi.org/10.1021/acsaem.0c01614.
[36] A. Gomez-Martin, J. Martinez-Fernandez, M. Ruttert, M. Winter, T. Placke, J. Ramirez-Rico, Correlation of Structure and Performance of Hard Carbons as Anodes for Sodium Ion Batteries, Chem. Mater. 31 (2019) 7288–7299. https://doi.org/10.1021/acs.chemmater.9b01768.
[37] P. Liu, Y. Li, Y.S. Hu, H. Li, L. Chen, X. Huang, A waste biomass derived hard carbon as a high-performance anode material for sodium-ion batteries, J. Mater. Chem. A. 4 (2016) 13046–13052. https://doi.org/10.1039/c6ta04877c.
[38] C. Bommier, W. Luo, W.Y. Gao, A. Greaney, S. Ma, X. Ji, Predicting capacity of hard carbon anodes in sodium-ion batteries using porosity measurements, Carbon N. Y. 76 (2014) 165–174. https://doi.org/10.1016/j.carbon.2014.04.064.
[39] W. Luo, C. Bommier, Z. Jian, X. Li, R. Carter, S. Vail, Y. Lu, J.J. Lee, X. Ji, Low-surface-area hard carbon anode for Na-ion batteries via graphene oxide as a dehydration agent, ACS Appl. Mater. Interfaces. 7 (2015) 2626–2631. https://doi.org/10.1021/am507679x.
[40] J.K. Mathiesen, R. Väli, M. Härmas, E. Lust, J. Fold Von Bülow, K.M.Ø. Jensen, P. Norby, Following the in-plane disorder of sodiated hard carbon through: Operando total scattering, J. Mater. Chem. A. 7 (2019) 11709–11717. https://doi.org/10.1039/c9ta02413a.
[41] W. Luo, J. Schardt, C. Bommier, B. Wang, J. Razink, J. Simonsen, X. Ji, Carbon nanofibers derived from cellulose nanofibers as a long-life anode material for rechargeable sodium-ion batteries, J. Mater. Chem. A. 1 (2013) 10662–10666. https://doi.org/10.1039/c3ta12389h.
[42] V. Simone, A. Boulineau, A. de Geyer, D. Rouchon, L. Simonin, S. Martinet, Hard carbon derived from cellulose as anode for sodium ion batteries: Dependence of electrochemical properties on structure, J. Energy Chem. 25 (2016) 761–768. https://doi.org/10.1016/j.jechem.2016.04.016.
[43] J. Jin, B.J. Yu, Z.Q. Shi, C.Y. Wang, C. Bin Chong, Lignin-based electrospun carbon nanofibrous webs as free-standing and binder-free electrodes for sodium ion batteries, J. Power Sources. 272 (2014) 800–807. https://doi.org/10.1016/j.jpowsour.2014.08.119.
[44] A. Kamiyama, K. Kubota, T. Nakano, S. Fujimura, S. Shiraishi, H. Tsukada, S. Komaba, High-Capacity Hard Carbon Synthesized from Macroporous Phenolic Resin for Sodium-Ion and Potassium-Ion Battery, ACS Appl. Energy Mater. 3 (2020) 135–140.

https://doi.org/10.1021/acsaem.9b01972.
[45] Y. Sun, P. Lu, X. Liang, C. Chen, H. Xiang, High-yield microstructure-controlled amorphous carbon anode materials through a pre-oxidation strategy for sodium ion batteries, J. Alloys Compd. 786 (2019) 468–474. https://doi.org/10.1016/j.jallcom.2019.01.388.
[46] A. Beda, P.L. Taberna, P. Simon, C. Matei Ghimbeu, Hard carbons derived from green phenolic resins for Na-ion batteries, Carbon N. Y. 139 (2018) 248–257. https://doi.org/10.1016/j.carbon.2018.06.036.
[47] G. Hasegawa, K. Kanamori, N. Kannari, J.I. Ozaki, K. Nakanishi, T. Abe, Studies on electrochemical sodium storage into hard carbons with binder-free monolithic electrodes, J. Power Sources. 318 (2016) 41–48. https://doi.org/10.1016/j.jpowsour.2016.04.013.
[48] A. Beda, F. Rabuel, M. Morcrette, S. Knopf, P.L. Taberna, P. Simon, C. Matei Ghimbeu, Hard carbon key properties allow for the achievement of high Coulombic efficiency and high volumetric capacity in Na-ion batteries, J. Mater. Chem. A. 9 (2021) 1743–1758. https://doi.org/10.1039/d0ta07687b.
[49] Y. Lu, C. Zhao, X. Qi, Y. Qi, H. Li, X. Huang, L. Chen, Y.S. Hu, Pre-Oxidation-Tuned Microstructures of Carbon Anodes Derived from Pitch for Enhancing Na Storage Performance, Adv. Energy Mater. 8 (2018) 1–6. https://doi.org/10.1002/aenm.201800108.
[50] C.D.M. Saavedra Rios, L. Simonin, A. De Geyer, C.M. Ghimbeu, C. Dupont, Unraveling the properties of biomass-derived hard carbons upon thermal treatment for a practical application in na-ion batteries, Energies. 13 (2020). https://doi.org/10.3390/en13143513.
[51] L. Wu, D. Buchholz, C. Vaalma, G.A. Giffin, S. Passerini, Apple-Biowaste-Derived Hard Carbon as a Powerful Anode Material for Na-Ion Batteries, ChemElectroChem. 3 (2016) 292–298. https://doi.org/10.1002/celc.201500437.
[52] X. Dou, C. Geng, D. Buchholz, S. Passerini, Research Update: Hard carbon with closed pores from pectin-free apple pomace waste for Na-ion batteries, APL Mater. 6 (2018). https://doi.org/10.1063/1.5013132.
[53] X. Dou, I. Hasa, M. Hekmatfar, T. Diemant, R.J. Behm, D. Buchholz, S. Passerini, Pectin, Hemicellulose, or Lignin? Impact of the Biowaste Source on the Performance of Hard Carbons for Sodium-Ion Batteries, ChemSusChem. 10 (2017) 2668–2676. https://doi.org/10.1002/cssc.201700628.
[54] A. Beda, J.M. Le Meins, P.L. Taberna, P. Simon, C. Matei Ghimbeu, Impact of biomass inorganic impurities on hard carbon properties and performance in Na-ion batteries, Sustain. Mater. Technol. 26 (2020). https://doi.org/10.1016/j.susmat.2020.e00227.
[55] Y.E. Zhu, H. Gu, Y.N. Chen, D. Yang, J. Wei, Z. Zhou, Hard carbon derived from corn straw piths as anode materials for sodium ion batteries, Ionics (Kiel). 24 (2018) 1075–1081. https://doi.org/10.1007/s11581-017-2260-1.
[56] K. Wang, Y. Jin, S. Sun, Y. Huang, J. Peng, J. Luo, Q. Zhang, Y. Qiu, C. Fang, J. Han, Low-Cost and High-Performance Hard Carbon Anode Materials for Sodium-Ion Batteries, ACS Omega. 2 (2017) 1687–1695. https://doi.org/10.1021/acsomega.7b00259.
[57] C. Nita, B. Zhang, J. Dentzer, C. Matei Ghimbeu, Hard carbon derived from coconut shells, walnut shells, and corn silk biomass waste exhibiting high capacity for Na-ion batteries, J. Energy Chem. 58 (2021) 207–218. https://doi.org/10.1016/j.jechem.2020.08.065.

[58] A. Pistone, C. Espro, Current trends on turning biomass wastes into carbon materials for electrochemical sensing and rechargeable battery applications, Curr. Opin. Green Sustain. Chem. 26 (2020) 100374. https://doi.org/10.1016/j.cogsc.2020.100374.
[59] J. Górka, C. Vix-Guterl, C. Matei Ghimbeu, Recent Progress in Design of Biomass-Derived Hard Carbons for Sodium Ion Batteries, C. 2 (2016) 24. https://doi.org/10.3390/c2040024.
[60] C. del M. Saavedra Rios, V. Simone, L. Simonin, S. Martinet, C. Dupont, Biochars from various biomass types as precursors for hard carbon anodes in sodium-ion batteries, Biomass and Bioenergy. 117 (2018) 32–37. https://doi.org/10.1016/j.biombioe.2018.07.001.
[61] G. Tondi, V. Fierro, A. Pizzi, A. Celzard, Tannin-based carbon foams, Carbon N. Y. 47 (2009) 1480–1492. https://doi.org/10.1016/j.carbon.2009.01.041.
[62] A. Celzard, V. Fierro, "Green", innovative, versatile and efficient carbon materials from polyphenolic plant extracts, Carbon N. Y. 167 (2020) 792–815. https://doi.org/10.1016/j.carbon.2020.05.053.
[63] A. Szczurek, V. Fierro, A. Pizzi, A. Celzard, Mayonnaise, whipped cream and meringue, a new carbon cuisine, Carbon N. Y. 58 (2013) 245–248. https://doi.org/10.1016/j.carbon.2013.02.056.
[64] A. Castro-Muñiz, S. Lorenzo-Fierro, A. Martínez-Alonso, J.M.D. Tascón, V. Fierro, F. Suárez-García, J.I. Paredes, Ordered mesoporous carbons obtained from low-value coal tar products for electrochemical energy storage and water remediation, Fuel Process. Technol. 196 (2019). https://doi.org/10.1016/j.fuproc.2019.106152.
[65] R.L.S. Canevesi, A. Sanchez-Sanchez, P. Gadonneix, A. Celzard, V. Fierro, Hierarchical tannin-derived carbons as efficient tetracycline adsorbents, Appl. Surf. Sci. 533 (2020) 0–39. https://doi.org/10.1016/j.apsusc.2020.147428.
[66] G. Tondi, W. Zhao, A. Pizzi, G. Du, V. Fierro, A. Celzard, Tannin-based rigid foams: A survey of chemical and physical properties, Bioresour. Technol. 100 (2009) 5162–5169. https://doi.org/10.1016/j.biortech.2009.05.055.
[67] K. Jurkiewicz, Ł. Hawełek, K. Balin, J. Szade, F.L. Braghiroli, V. Fierro, A. Celzard, A. Burian, Conversion of Natural Tannin to Hydrothermal and Graphene-Like Carbons Studied by Wide-Angle X-ray Scattering, J. Phys. Chem. A. 119 (2015) 8692–8701. https://doi.org/10.1021/acs.jpca.5b02407.
[68] W. Zhao, A. Pizzi, V. Fierro, G. Du, A. Celzard, Effect of composition and processing parameters on the characteristics of tannin-based rigid foams. Part I: Cell structure, Mater. Chem. Phys. 122 (2010) 175–182. https://doi.org/10.1016/j.matchemphys.2010.02.062.
[69] M. Letellier, A. Szczurek, M.C. Basso, A. Pizzi, V. Fierro, O. Ferry, A. Celzard, Preparation and structural characterisation of model cellular vitreous carbon foams, Carbon N. Y. 112 (2017) 208–218. https://doi.org/10.1016/j.carbon.2016.11.017.
[70] P. Mallet-Ladeira, PhD Thesis, Analyse multiéchelle de carbones pyrolytiques, Université Toulouse 3 Paul Sabatier, France, September 2014.
[71] P. Mallet-Ladeira, P. Puech, C. Toulouse, M. Cazayous, N. Ratel-Ramond, P. Weisbecker, G.L. Vignoles, M. Monthioux, A Raman study to obtain crystallite size of carbon materials: A better alternative to the Tuinstra-Koenig law, Carbon N. Y. 80 (2014) 629–639. https://doi.org/10.1016/j.carbon.2014.09.006.
[72] J. Jagiello, J. Kenvin, C.O. Ania, J.B. Parra, A. Celzard, V. Fierro, Exploiting the adsorption of simple gases O2 and H2 with minimal quadrupole moments for the dual

gas characterization of nanoporous carbons using 2D-NLDFT models, Carbon N. Y. 160 (2020) 164–175. https://doi.org/10.1016/j.carbon.2020.01.013.
[73] A. Sanchez-Sanchez, M.T. Izquierdo, S. Mathieu, G. Medjahdi, V. Fierro, A. Celzard, Activated carbon xerogels derived from phenolic oil: Basic catalysis synthesis and electrochemical performances, Fuel Process. Technol. 205 (2020) 106427. https://doi.org/10.1016/j.fuproc.2020.106427.
[74] A. Celzard, A. Pasc, S. Schaefer, K. Mandel, T. Ballweg, S. Li, G. Medjahdi, V. Nicolas, V. Fierro, Floating hollow carbon spheres for improved solar evaporation, Carbon N. Y. 146 (2019) 232–247. https://doi.org/10.1016/j.carbon.2019.01.101.
[75] D.A. Stevens, J.R. Dahn, An In Situ Small-Angle X-Ray Scattering Study of Sodium Insertion into a Nanoporous Carbon Anode Material within an Operating Electrochemical Cell, J. Electrochem. Soc. 147 (2000) 4428. https://doi.org/10.1149/1.1394081.
[76] C. Bommier, D. Leonard, Z. Jian, W.F. Stickle, P.A. Greaney, X. Ji, New Paradigms on the Nature of Solid Electrolyte Interphase Formation and Capacity Fading of Hard Carbon Anodes in Na-Ion Batteries, Adv. Mater. Interfaces. 3 (2016). https://doi.org/10.1002/admi.201600449.
[77] D.I. Iermakova, R. Dugas, M.R. Palacín, A. Ponrouch, On the Comparative Stability of Li and Na Metal Anode Interfaces in Conventional Alkyl Carbonate Electrolytes, J. Electrochem. Soc. 162 (2015) A7060–A7066. https://doi.org/10.1149/2.0091513jes.
[78] A. Rudola, D. Aurbach, P. Balaya, A new phenomenon in sodium batteries: Voltage step due to solvent interaction, Electrochem. Commun. 46 (2014) 56–59. https://doi.org/10.1016/j.elecom.2014.06.008.
[79] A. Ponrouch, D. Monti, A. Boschin, B. Steen, P. Johansson, M.R. Palacín, Non-aqueous electrolytes for sodium-ion batteries, J. Mater. Chem. A. 3 (2015) 22–42. https://doi.org/10.1039/c4ta04428b.
[80] Y. Wang, Z. Feng, W. Zhu, V. Gariépy, C. Gagnon, M. Provencher, D. Laul, R. Veillette, M.L. Trudeau, A. Guerfi, K. Zaghib, High capacity and high efficiency maple tree-biomass-derived hard carbon as an anode material for sodium-ion batteries, Materials (Basel). 11 (2018). https://doi.org/10.3390/ma11081294.